

## PHYSICS

# Influence of atomic-scale defects on coherent phonon excitations by THz near fields in an STM

Vibhuti N. Rai<sup>1\*</sup>, Junyoung Sim<sup>1</sup>, Florian Faaber<sup>1</sup>, Nils Bogdanoff<sup>1</sup>, Sergey Trishin<sup>1</sup>, Paul Wiechers<sup>1</sup>, Tom S. Seifert<sup>1</sup>, Tobias Kampfrath<sup>2</sup>, Christian Lotze<sup>1</sup>, Katharina J. Franke<sup>2</sup>

Coherent phonons describe the collective, ultrafast motion of atoms and play a central role in light-induced structural dynamics. Here, we use terahertz (THz) scanning tunneling microscopy to excite and detect coherent phonons in semiconducting 2H-MoTe<sub>2</sub> and resolve how their excitation is influenced by atomic-scale defects. In a THz pump-probe scheme, we observe long-lived oscillatory signals that we assign to out-of-plane breathing and in-plane shear modes, which are both dipole forbidden in the bulk. The relative excitation strength of these modes varies near defects, indicating that tip-induced local band bending modulates the coupling to the THz field. This defect-tunable coupling offers previously unidentified opportunities to control selective excitation of vibrational modes at the nanoscale.

## INTRODUCTION

The ultrafast motion of atoms governs many fundamental properties of materials, such as heat, charge, and spin transport, owing to the coupling between the different degrees of freedom. Coherent phonons are particularly interesting as they are phase-locked lattice vibrations that can provide direct insight into light-induced structural changes, electron/exciton-phonon interaction, and nonlinear lattice dynamics, while also offering a way to actively modify electronic properties (1–7). The role of coherent lattice dynamics becomes especially important for engineering nanoscale devices based on (quasi) two-dimensional systems such as transition-metal dichalcogenides. Their pronounced light-matter interactions enhance coherent phonon generation and enable ultrafast structural phase transitions by optical and terahertz (THz) pulses.

A major advantage of the THz regime is that lattice dynamics can be driven resonantly and efficiently without substantial heating (8–13), enabling access to nonthermal pathways for controlling structural and electronic properties. Driving by THz pulses is intriguingly versatile because it allows for the excitation of different phonon modes via various direct and indirect mechanisms (14–17). Ideally, one would like to selectively address certain modes by the THz pulses, potentially allowing for tuning material properties and enhancing the efficiency of driving phase transitions. However, unavoidable intrinsic defects may interact with the phonon modes and modify their properties (18). Understanding the interaction of phonons with single defects requires a technique with both atomic-scale spatial and ultrafast temporal resolution. Furthermore, understanding the role of defects on phonon dynamics at the atomic scale highlights a pathway to engineer phonon excitations by selectively introducing defects into nanoscale materials.

A breakthrough toward the resolution of atomic-scale dynamics has been achieved by the development of THz scanning tunneling microscopy (THz-STM), often referred as lightwave-driven STM (see Fig. 1A) (19, 20). Here, a THz pulse is coupled into an STM junction, enabling field-enhanced time-resolved spectroscopy with

atomic-scale spatial resolution in a pump-probe scheme (11, 19–28). In essence, a phase-stable, single-cycle THz pulse adds an ultrafast oscillating bias voltage to the static dc bias voltage applied between the tip and the sample. This pulse leads to a transient change in the conductance, with its temporal evolution being probed by a second time-delayed pulse. By measuring the dc response, this THz pump-probe scheme enables spatially resolved investigations of dynamical processes. Recently, this method has been used to address key questions in condensed matter physics, including charge carrier dynamics (19, 22, 24, 29), charge-density-wave dynamics (27), and even phase transitions (11). The THz field in the STM junction has also been used to excite and probe single-molecule properties (20, 28, 30) and localized vibrational modes at atomic-scale defects (13, 31) and to launch and detect acoustic phonons via their reflections at material interfaces (32).

Despite these advances, the excitation and detection of intrinsic, long-range coherent optical phonons using THz-STM has remained elusive. Efficient coupling of a THz pulse requires a polarization that can oscillate at THz frequencies. In semiconductors, surface band bending and inefficient screening of external fields lead to charge separation that can be dynamically modulated by the THz field, resulting in a transient dipole moment that couples to the driving field.

Here, we use the near-field THz enhancement in the nanocavity of an STM tip and a semiconducting 2H-MoTe<sub>2</sub> surface to locally excite and detect coherent phonon modes. Surface symmetry breaking and tip- and field-induced band bending allow us to address phonon modes that are forbidden in the bulk. Even more interestingly, we observe that atomic defects modify the intensity of the excited modes in the phonon spectral density. We attribute the selective enhancement to different transient dipoles in the presence of the defects due to transient charging in response to the local band bending.

## RESULTS

2H-MoTe<sub>2</sub> has a trigonal prismatic structure, where each molybdenum (Mo) atom is sandwiched between two tellurium (Te) atoms, forming a MoTe<sub>2</sub> layer (see Fig. 1B). These layers are stacked along the *c* axis by van der Waals interactions leading to inversion symmetry in the bulk crystal structure. Figure 1C shows a typical STM topography of 2H-MoTe<sub>2</sub> surface. The terraces are atomically flat

Copyright © 2025 The Authors, some rights reserved; exclusive licensee American Association for the Advancement of Science. No claim to original U.S. Government Works. Distributed under a Creative Commons Attribution NonCommercial License 4.0 (CC BY-NC).

<sup>1</sup>Fachbereich Physik, Freie Universität Berlin, Arnimallee 14, 14195 Berlin, Germany.

<sup>2</sup>Fachbereich Physik and Halle–Berlin–Regensburg Cluster of Excellence CCE, Freie Universität Berlin, Arnimallee 14, 14195 Berlin, Germany.

\*Corresponding author. Email: vibhuti.raif@fu-berlin.de

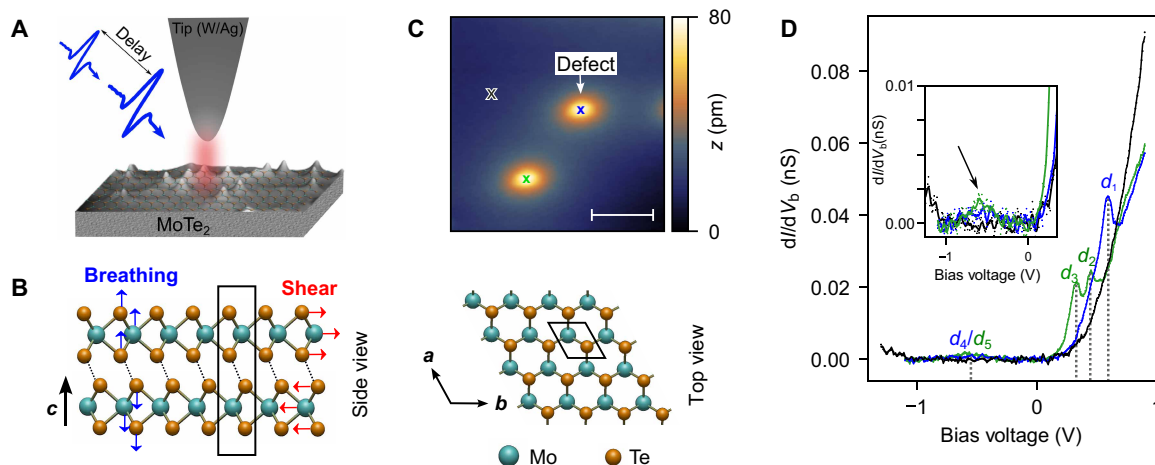


**Fig. 1. STM characterization of 2H-MoTe<sub>2</sub>.** (A) Sketch illustrating the coupling of THz pulses into the STM junction (not to scale). (B) Side view and top view of MoTe<sub>2</sub> in the 2H-phase (not to scale). In-plane ( $E_{2g}^z$ ) and out-of-plane ( $B_{2g}^z$ ) vibrational motions are shown with red and blue arrows, respectively. (C) STM topography of the in-situ cleaved 2H-MoTe<sub>2</sub>. Tunneling parameters for recording the topography are  $V_b = 1.3$  V, and  $I = 20$  pA. Scale bar, 5 nm. (D)  $dI/dV_b$  spectra recorded on the pristine surface (in black) and on two defects (in blue and green) (feedback opened at  $V_b = 0.9$  V,  $I = 20$  pA, and  $V_{mod} = 13$  mV). The tip positions are marked with colored crosses (black, blue, and green) in (C). Positions of the defect states ( $d_1$  to  $d_5$ ) for the two defects are indicated by the vertical dashed lines. The inset shows a close-up view on the negative part of the gap, bringing out the deep in-gap defect state, marked with a black arrow. All defect states are labeled  $d_i$ .

but with occasional protrusions that can be attributed to intrinsic defects such as substitutional sites or vacancies (see note S1 for sample preparation) (33). The differential conductance measurement ( $dI/dV_b$ ) on the pristine area shows a gap of around 1.2 eV (black curve in Fig. 1D), consistent with the semiconducting nature and previous measurements (34–36). The defect sites exhibit several in-gap states (Fig. 1D). Depending on the specific type of defects, there are one or two states close to the conduction band (CB), i.e., at  $V_b \approx 0.60$  V ( $d_1$  in the blue curve) and  $V_b \approx 0.32$  V and  $V_b \approx 0.44$  V ( $d_2$  and  $d_3$  in the green curve), respectively. In addition, both sites show a broad defect state at  $V_b \approx -0.60$  V ( $d_4/d_5$ ) near the valence band. As we will show later, charging the defect states will have a crucial impact on the phonon excitation probability.

### THz-STM

To investigate the phonon dynamics, the STM junction is irradiated with THz pulses (Fig. 1A). Two phase-stable, single-cycle THz pulses are generated by irradiating a LiNbO<sub>3</sub> crystal with a pair of infrared (IR) pulses of 1030 nm wavelength and 300 fs duration (see note S2 for more details) (37–39). It is essential to accurately characterize the near-field THz waveform in the STM junction, as reflections and low-pass filtering can distort the pulse and obscure the true dynamics of the system (40, 41). We first verify the generation of a single-cycle THz pulse and determine its free-space field strength using electro-optic sampling (EOS) outside the junction (for the EOS details, see notes S2 and S3). This pulse  $E_{THz}^{inc}$  is subsequently coupled into a junction consisting of a silver (Ag)-covered tungsten tip in front of a 2H-MoTe<sub>2</sub> sample for in-junction characterization. The generated and coupled THz pulses are linearly polarized along the tip axis. To probe the pulse shape within the junction, we use a second-harmonic pulse (515 nm) of the IR laser to induce photoemission, which is subsequently modulated by the time-delayed THz field  $E_{THz}^{inc}$ . For these measurements, the tip is held several micrometers away from the surface (for details, see note S3). The signal confirms the single-cycle nature of the THz pulse as shown in Fig. 2A

and fig. S3 (24, 40, 42–44). The Fourier transform of the signal shows the bandwidth of the pulse with a central frequency of  $\approx 0.5$  THz and a strong spectral-weight cutoff above  $\approx 1.0$  THz (Fig. 2B).

With the THz pulse shape and free-space strength  $E_{THz}^{inc}$  characterized, we now use it as a transient bias voltage ( $V_{THz}$ ) for ultrafast measurements in the tunneling regime. Owing to the field enhancement in the Ag–MoTe<sub>2</sub> junction, the amplitude of  $V_{THz}$  must first be calibrated. In the presence of the THz pulse, the transient bias voltage  $V_{THz}(t)$  adds to the applied dc bias voltage  $V_b$ , such that the total voltage at the junction is  $V(t) = V_b + V_{THz}(t)$ . The resulting THz-induced current  $I_{THz} = R_{rate} \times \int i_{THz}(t) dt$  is measured as a modulation of the dc tunneling current with a lock-in amplifier (because the transimpedance amplifier cannot follow the sub-picosecond transient current  $i_{THz}(t)$ ; for details, see note S5). The amplitude of the transient voltage  $V_{THz}(t)$  is tuned by changing  $E_{THz}^{inc}$  using a pair of wire grid polarizers (for details, see note S2). In the absence of THz excitation ( $E_{THz}^{inc} = 0$ ), no additional current  $I_{THz}$  is detected, and only the static  $I(V_b)$  is measured (black trace in Fig. 2C). At  $E_{THz}^{inc} = 0.2$  kV/m, a small induced current appears (red trace), with an onset close to that of the static  $I(V_b)$ . Increasing the far-field  $E_{THz}^{inc}$  to 2.1 kV/m shifts the onset of  $I_{THz}$  below the static CB minimum, corresponding to a transient bias voltage  $V_{THz} \approx 260$  mV (Fig. 2C). In the following, we use this amplitude for the probe pulse, while the pump pulse is of 325 mV. These moderate field strengths are chosen to avoid strong modification of the poorly screened electronic band structure of the semiconducting MoTe<sub>2</sub> (31, 45, 46), while still yielding sufficiently strong signals and efficient phonon coupling.

### THz response of MoTe<sub>2</sub>

The two THz pulses described above are time-delayed with respect to each other to excite and probe the phonons in 2H-MoTe<sub>2</sub>. The pump pulse excites the sample by locally perturbing the substrate via its electric field, inducing an a priori unknown dynamics, which is subsequently measured by the probe pulse as a function of the time delay ( $\tau$ ) between the two THz pulses. Figure 3A shows four

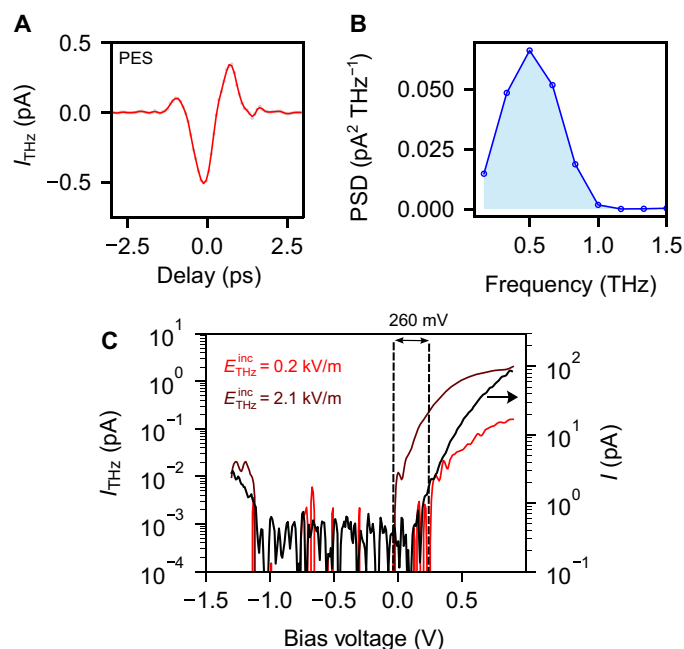


**Fig. 2. THz pulse shape in the STM junction.** (A) Near-field pulse shape measured by photoemission sampling by a Ag tip in front of a 2H-MoTe<sub>2</sub> surface. Parameters for acquiring the pulse shape,  $V_b = -5.0$  V, laser repetition rate  $R_{\text{rate}} = 1.25$  MHz. (B) Power spectral density (PSD) from Fast Fourier transform of the THz pulse shown in (A). (C) THz-induced tunneling current ( $I_{\text{THz}}$ ) as a function of  $V_b$  at two different  $E_{\text{THz}}^{\text{inc}}$  (feedback opened at  $V_b = 0.9$  V and  $I = 20$  pA). The signal is integrated for 0.5 s at each data point at a pulse repetition rate  $R_{\text{rate}} = 10$  MHz. For comparison, the dc current is shown (in black) without any THz field.

time traces taken at different dc bias voltages on the pristine surface, exhibiting a voltage-dependent oscillatory signal that lasts up to 50 ps. The signal is strongly modulated over the measured time window, suggesting the presence of more than one frequency component. In contrast to the strong oscillatory signal at  $V_b = 0.6$  V, the equivalent measurements acquired with a dc bias inside the semiconducting bandgap show no signal (traces at  $V_b = -0.2$  V and  $-0.6$  V in Fig. 3A). To understand the origin of the signal, we consider the effect of the two time-delayed pulses, both delivering an electric field to the junction, which is amplified at the tip apex by several orders of magnitude as has been calibrated above (20, 22, 47). The first THz pulse (pump) initiates a coherent process, the dynamics of which are probed by the second pulse (probe). This leads to  $I_{\text{THz}}$ , which is only measurable if the material is sufficiently conductive at the transient bias voltage, i.e., when  $V_{\text{THz,probe}}$  is sufficiently strong to reach the edge of the bandgap of 2H-MoTe<sub>2</sub>. As a result, no signal is observed at  $V_b$  deep within the bandgap, consistent with our estimated amplitude  $V_{\text{THz}}$  above. Consequently, the traces at  $V_b = -0.2$  V and  $-0.6$  V show no induced current.

We now aim to understand the origin of the long-lasting oscillations of  $I_{\text{THz}}$  upon reaching the CB. We first note that the oscillatory signal cannot originate solely from the convolution of the two THz pulses with the nonlinear static  $I(V_b)$ , i.e., without involving any substrate dynamics. This is confirmed by calculating the induced current  $I_{\text{THz}}$  for two time-delayed pulses (see note S5), which differs clearly from the experimental traces. Consequently, the traces must

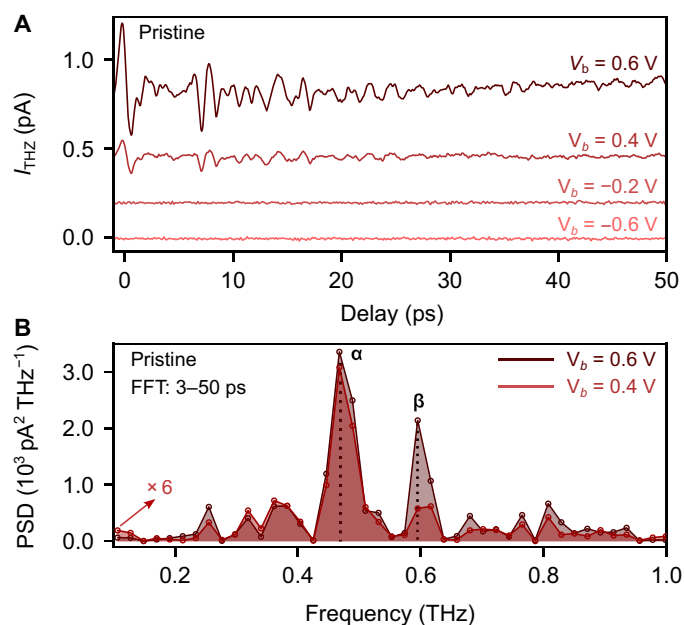


**Fig. 3. Terahertz pump-probe measurements on pristine 2H-MoTe<sub>2</sub>.** (A) Time traces of THz-induced tunneling current ( $I_{\text{THz}}$ ) on the pristine region at different bias voltages (feedback opened at  $V_b = 0.9$  V,  $I = 10$  pA, and  $R_{\text{rate}} = 10$  MHz). Traces are offset in increasing amount for clarity. (B) PSD obtained from the FFT of  $I_{\text{THz}}$  traces shown in (A). The range for the FFT is from 3 to 50 ps, which was chosen to avoid the dominant nonlinearities at ultrafast timescales.

include a dynamical process within the sample. To resolve the frequencies of the induced excitations, we perform the fast Fourier transform (FFT) (Fig. 3B) and look at the power spectral density (PSD). For the FFT, we excluded the overlap region of the two pulses, where ultrafast processes, typically related to hot electron dynamics or other processes, such as Zener tunneling and impact ionization (48, 49), are beyond our time resolution. Instead, we are interested in long-lasting dynamics (for analysis details, see note S4). The FFT reveals two prominent peaks with high spectral weights at 0.48 THz (labeled  $\alpha$ ) and 0.6 THz (labeled  $\beta$ ). The low-intensity side peaks exhibit no notable variation with applied bias voltage or local defects (discussed later). The clear observation of sharp peaks signifies coherent excitations that we attribute to phonons due to their energy range being compatible with phonon modes of bulk 2H-MoTe<sub>2</sub> (50–53). Group theory predicts three acoustic ( $E_{1u}^1$  and  $A_{2u}^1$ ) and 15 optical phonon modes for bulk 2H-MoTe<sub>2</sub>. Among the optical modes, five are doubly degenerate in-plane and another five are nondegenerate out-of-plane modes at the  $\Gamma$  point, but disperse and split away from it, as reported in previous studies (50, 53). With the THz pulse being confined below the tip, coupling of the transient electric field to modes close but not restricted to zero momentum, i.e., to the  $\Gamma$  point, is possible. On the basis of their frequencies, we tentatively assign our observed  $\alpha$  and  $\beta$  modes to the in-plane shear  $E_{2g}^2$  mode and the out-of-plane breathing  $B_{2g}^2$  mode, respectively, though we note that prior experimental and theoretical values depend on the precise conditions prohibiting the assignment based on the precise phonon frequencies (50, 51, 53, 54). These modes are Raman active; however, contrary to the bulk 2H-MoTe<sub>2</sub>, inversion symmetry is broken at the surface, potentially rendering these also IR active.

## DISCUSSION

To understand the excitation, we note that coherent phonons can be generated through three primary mechanisms: (i) impulsive stimulated Raman scattering (55, 56), which is a nonresonant process involving excitation of higher energy states and Stokes scattering; (ii) dispersive excitation of coherent phonons (57), which relies on resonant electronic excitations; or (iii) direct coupling of the THz electric pump field to the dipole moment of vibrational modes (58, 59). The first two mechanisms require substantially larger-energy pump pulses [or unlikely multiple photon absorption (17)] for any inter-band transitions than provided by our THz pulses, and can therefore be excluded. This indicates that a direct coupling of the electric field to a dynamic charge distribution at the surface resonantly excites the phonons, which are well within the bandwidth of our THz pulse. Regardless of the excitation mechanism, the detection of the phonon modes relies on conductance changes, which can be induced by both the in-plane  $E_{2g}^2$  mode and the out-of-plane breathing  $B_{2g}^2$  mode, as both influence the local density of states below the STM tip.

To gain further insight into the excitation mechanism and coupling efficiencies, we compare the time traces at  $V_b = 0.6$  V and  $V_b = 0.4$  V in more detail (see Fig. 3B). Though both traces show the oscillations, their intensity is reduced at 0.4 V compared to the larger dc voltage. The overall decrease can be attributed to the highly nonlinear  $I(V_b)$  curve, especially at the CB band onset, which effectively

modifies  $I_{\text{THz}}$  of the probe pulse (also see fig. S4). In contrast, the change in relative intensity of the  $\alpha$  and  $\beta$  mode with the  $\beta$  mode showing a stronger intensity reduction than the  $\alpha$  mode cannot be accounted for by the nonlinearity in the  $I(V_b)$  characteristics (see the calculated spectral response in note S5).

To understand the energy-dependent excitation strength of the two modes and identify opportunities for its control, we investigate the THz pump-probe response at the previously identified defect sites. To this end, we measured time traces on the defect shown above (blue curve in Fig. 1D) in different bias regimes. Figure 4 (A and B) displays four time traces and their corresponding FFT spectra acquired at different  $V_b$ . To ensure a meaningful comparison, the tip-sample distance was maintained similar to that used in the measurements on the pristine surface (Fig. 3A). At positive bias voltages, the FFT spectra match those observed in pristine regions (Fig. 3A), showing the two phonon modes,  $\alpha$  and  $\beta$ . The similarities in both the energy and relative intensities of the two modes suggest that the changes in the nonlinearity of the  $I(V_b)$  curve due to the defect states at positive  $V_b$  (green curve in Fig. 1D) have no major effect. However, the time trace measured at negative bias voltage displays a very different behavior. This becomes evident in the FFT signal (Fig. 4, B to D) as the relative intensity of the two modes is inverted with the  $\beta$  mode being more intense than the  $\alpha$  mode.

The inversion of the intensity of  $\alpha$  and  $\beta$  with different dc bias voltage and compared to the pristine surface cannot be explained by

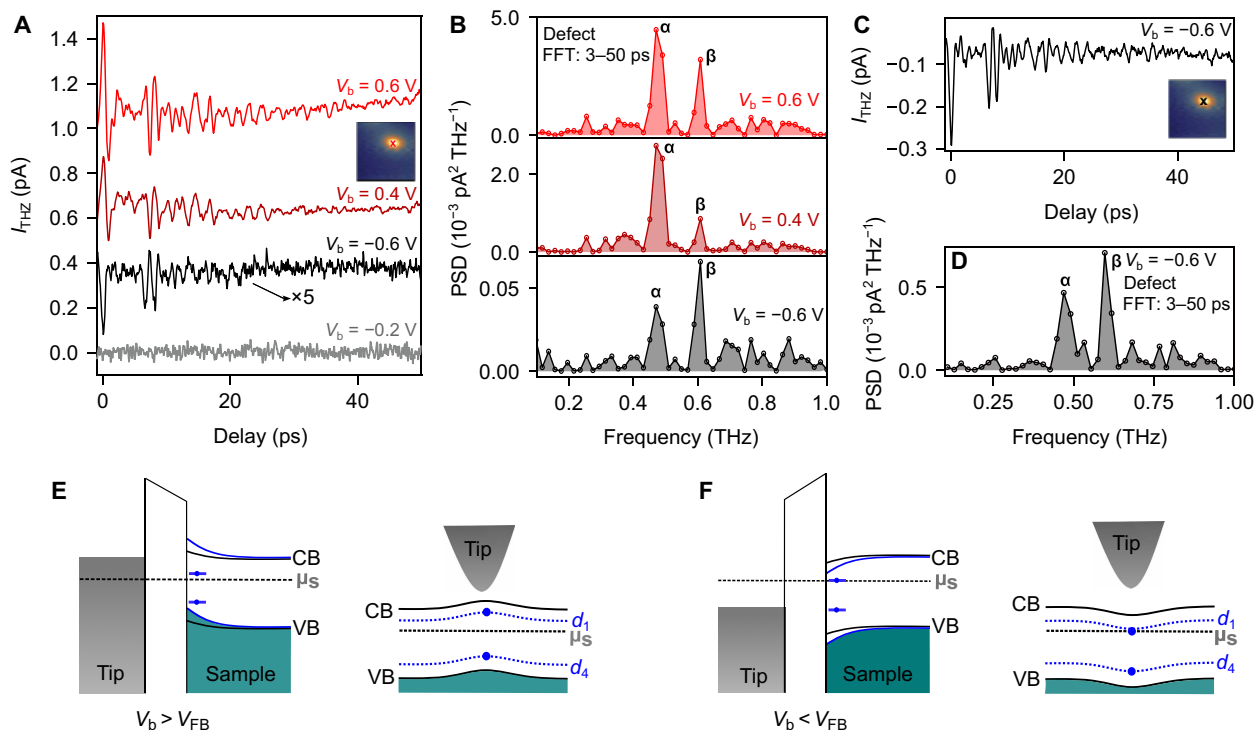


**Fig. 4. Effect of defects on the phonon modes.** (A) Time-resolved traces of  $I_{\text{THz}}$  recorded at different  $V_b$  (feedback opened at  $V_b = 0.9$  V,  $I = 30$  pA, and  $R_{\text{rate}} = 10$  MHz for all traces). Measurement positions of the time traces are marked with the (red) cross in the inset topography ( $V_b = 0.9$  V and  $I = 4$  pA). Traces are offset in increasing amount for clarity. (B) PSD obtained from the FFT of  $I_{\text{THz}}$  traces shown in (A). The range for the FFT is from 3 to 50 ps. (C) Time trace recorded on the same defect as in (A) but at closer tip sample distance (feedback opened at  $V_b = 0.6$  V and  $I = 30$  pA) and (D) the corresponding PSD. For all time-resolved traces, a repetition rate  $R_{\text{rate}} = 10$  MHz is used. The signal is integrated for 0.5 s at each data point. (E) Left: Energy diagram representing induced band bending at the surface of  $\text{MoTe}_2$  at  $V_b > V_{\text{FB}}$ , where  $V_{\text{FB}}$  is the flat-band condition. Black/blue solid line represents the band bending on the pristine/defect area. Right: Lateral profile of the energy bands below the STM tip. Two defect states ( $d_1$  and  $d_4$ ) are indicated by blue dots. (F) Left: Energy diagram at  $V_b < V_{\text{FB}}$ . Right: Lateral profile of the energy bands below the STM tip. In both (E) and (F), dotted black and blue lines represent the chemical potential and defect state, respectively.

a simple spectral response of the two THz pulses interacting with the nonlinear static  $I(V_b)$  curve, even in the presence of the in-gap state at  $V_b = -0.6$  V (for calculated spectra, see note S5). Instead, to explain this behavior, we consider the transient charge distribution at the surface and how this may influence the excitation efficiency. The total electric field in the junction consists of the tip-induced band bending  $E_{BB}$  due to the difference in the work functions of the tip and the sample, the applied dc electric field  $E_{DC}$ , and the THz field  $E_{THz}(t)$ :  $E_{tot} = E_{THz}(t) + E_{DC} + E_{BB}$ . We note that it is nontrivial to determine  $E_{BB}$  in an STM junction. Because the work functions of Ag (4.2 to 4.7 eV, depending on crystallographic termination of the tip) and 2H-MoTe<sub>2</sub> (4.1 to 4.4 eV) are nearly the same (60, 61),  $E_{BB}$  is expected to be small.

To illustrate the tip- and field-induced dipole, we present energy diagrams for two regimes at either side of the flat band ( $V_{FB}$ ) condition (Fig. 4, E and F). In both cases, the applied bias voltage shifts the band relative to the flat-band condition, where the work function difference between tip and the sample is compensated by the applied  $V_b$ .

For  $V_b > V_{FB}$  (Fig. 4E), the bands bend upward, creating a charge depletion region at the MoTe<sub>2</sub> surface and a surface dipole. The THz electric field couples to the Mo and Te ions via Coulomb interaction, accelerates them, and thus triggers coherent ionic vibrations (phonons). Because of the dc bias voltage variation, the static charge distribution is modified, which also modifies the effective charge of the ions and, thus, the phonon excitation efficiency. While we cannot make any quantitative statements on the charge distributions, this model captures the changes on the (relative) intensities of the phonon modes on the pristine surface.

In this band alignment, the defect states at positive bias voltage ( $d_1$ ) have only a slight effect on the charge distribution and, consequently, on the excitation of the in-plane shear and out-of-plane breathing modes. Likewise, occupied defect states at negative bias do not alter the local charge distribution substantially as long as they remain below the chemical potential. As a result, the phonon spectra of defect and pristine areas are similar at positive bias voltage (Fig. 3).

In contrast, for  $V_b < V_{FB}$ , the MoTe<sub>2</sub> band bends downward at the interface (Fig. 4F), again inducing a surface charge accumulation. At sufficiently strong band bending, the occupied defect state at negative bias ( $d_1$ ) crosses the chemical potential, altering the charge state and, thereby, also the transient charges that determine the phonon excitation efficiency. This model explains that the  $\beta$  mode becomes more intense than the  $\alpha$  mode at  $V_b = -0.6$  V, indicating that the THz field excites the  $\beta$  mode more efficiently at the defect site than on the pristine surface. [We note that the strong unoccupied defect states ( $d_1$  to  $d_3$ ) are responsible for the different phonon excitation at negative bias voltage, rather than the defect states at negative bias voltage ( $d_4/d_5$ ). For comparison of a different defect, see note S7].

The inverse intensity ratio of the two phonon modes at the defect site compared to the pristine surface indicates that the in-plane shear and out-of-plane breathing mode respond differently to the local band bending at the defect site. The sketch of the profile of the band bending near the defect in Fig. 4F illustrates that there is a field component parallel to the surface, enhancing the inhomogeneity of the electric field in the STM junction (62). We ascribe the qualitatively different response of the two modes to this field profile.

Different defects introduce distinct in-gap states, which modify the in-plane field component. Accordingly, measurements on various

defects reveal different  $\alpha$ -to- $\beta$  ratios (see note S7). The balance between the out-of-plane and in-plane components depends on factors such as the defect type, tip-sample distance, and tip geometry. Although these complexities hinder a fully quantitative description, our findings indicate that the coupling to out-of-plane breathing and in-plane shear modes by an inhomogeneous electric field (31) can be locally tuned by defect-induced charge distributions.

Because the dc field scales with the tip-sample distance, the degree of band bending and, thus, the out-of-plane charge distribution varies accordingly. As shown in Fig. 4 (C and D), reducing the tip-sample distance alters the intensity ratio of the two phonon modes albeit not as pronounced as the presence of a defect compared to the pristine surface, where there are strong changes of the transient charging.

We used THz STM to study coherent phonon excitations in 2H-MoTe<sub>2</sub> with atomic-scale resolution. Time-resolved measurements revealed two distinct phonon modes whose relative excitation strength varies with bias voltage, but most notably locally in the presence of defects. This variation is attributed to tip-induced band bending and transient charging of defect states, which modulate the efficiency for coupling to in-plane and out-of-plane vibrational modes while leaving their frequency unchanged within our resolution.

Our results demonstrate that the local atomic structure influences coherent lattice dynamics and suggest that selective phonon excitation via local field engineering could offer a route to control material properties at the nanoscale.

## MATERIALS AND METHODS

Bulk 2H-MoTe<sub>2</sub> crystals (bought from HQ Graphene) are cleaved in an ultrahigh vacuum chamber at room temperature. After cleaving, the sample was cooled with liquid helium before being inserted into the STM operated at  $\approx 6$  K.

The STM tip was prepared by electrochemical etching of a tungsten wire. To achieve efficient coupling of optical light, the tip apex was sufficiently covered with silver by dipping the tip into a Ag(111) surface.

The optical setup is placed on a vibration-isolated optical table located next to the STM chamber. A sketch of the optical setup is shown in fig. S2. We use an IR laser (1030 nm, 350 fs, 50 W, Satsuma HP3 from Amplitude). The output laser power is divided into two parts: A small fraction of the laser power (0.5 to 8 W) is used for an optical pump pulse. This allows for characterization of the THz pulses through EOS and photoemission sampling (PES). The major power of the laser is further split into two parts by using a polarizing beam splitter. One beam is then delayed with respect to the other one. Both beams are focused on a LiNbO<sub>3</sub> crystal in tilted pulse-front geometry for the generation of two THz pulses (37, 38). The path length of the THz beams—from generation to coupling into the STM chamber—is kept as short as possible to minimize the effect of water absorption. The EOS setup is used for the calibration of the far-field THz strength ( $E_{THz}^{inc}$ ) (more details in note S3). For PES in the STM junction, the second harmonic is generated (515 nm) by a BBO (BaB<sub>2</sub>O<sub>4</sub>) crystal placed in the optical path.

For the THz pump-THz probe measurements, one of the beams (probe) is modulated by an optical chopper synchronized with a lock-in amplifier measuring the THz-induced tunneling current. Throughout this work, the chopper is operated at a frequency of 817 Hz unless mentioned otherwise. The second beam is delayed with respect to

the probe by a delay stage to achieve the pump-probe measurement scheme. Furthermore, the THz field strength is controlled by a pair of wire-grid polarizers. The first polarizer was rotated relative to the polarization of the generated THz beam to control the amplitude of the THz field, while the second polarizer defined the polarization of the THz radiation impinging on the STM junction.

To couple the THz pulses into an STM junction, a Besocke Beetle-style STM (CreaTec Fischer and Co.) was modified. In particular, this included modification of the radiation shields.

## Supplementary Materials

This PDF file includes:

Figs. S1 to S7

Notes S1 to S7

## REFERENCES AND NOTES

- M. Hase, M. Kitajima, S.-I. Nakashima, K. Mizoguchi, Dynamics of coherent anharmonic phonons in bismuth using high density photoexcitation. *Phys. Rev. Lett.* **88**, 067401 (2002).
- T. Y. Jeong, B. M. Jin, S. H. Rhim, L. Debbichi, J. Park, Y. D. Jang, H. R. Lee, D.-H. Chae, D. Lee, Y.-H. Kim, S. Jung, K. J. Yee, Coherent lattice vibrations in mono- and few-layer WSe<sub>2</sub>. *ACS Nano* **10**, 5560–5566 (2016).
- D. Rossi, L. E. Camacho-Forero, G. Ramos-Sánchez, J. H. Han, J. Cheon, P. Balbuena, D. H. Son, Anisotropic electron-phonon coupling in colloidal layered TiS<sub>2</sub> nanodiscs observed via coherent acoustic phonons. *J. Phys. Chem. C* **119**, 7436–7442 (2015).
- Y. Zhang, X. Shi, W. You, Z. Tao, Y. Zhong, F. Cheenicode Kabeer, P. Maldonado, P. M. Oppeneer, M. Bauer, K. Rossnagel, H. Kapteyn, M. Murnane, Coherent modulation of the electron temperature and electron-phonon couplings in a 2D material. *Proc. Natl. Acad. Sci. U.S.A.* **117**, 8788–8793 (2020).
- E. J. Sie, C. M. Nyby, C. D. Pemmaraju, S. J. Park, X. Shen, J. Yang, M. C. Hoffmann, B. K. Ofori-Okai, R. Li, A. H. Reid, S. Weathersby, E. Mannebach, N. Finney, D. Rhodes, D. Chenet, A. Antony, L. Balicas, J. Hone, T. P. Devereaux, T. F. Heinz, X. Wang, A. M. Lindenberg, An ultrafast symmetry switch in a Weyl semimetal. *Nature* **565**, 61–66 (2019).
- B. He, C. Zhang, W. Zhu, Y. Li, S. Liu, X. Zhu, X. Wu, X. Wang, H.-H. Wen, M. Xiao, Coherent optical phonon oscillation and possible electronic softening in WTe<sub>2</sub> crystals. *Sci. Rep.* **6**, 30487 (2016).
- C. Li, A. V. Scherbakov, P. Soubelet, A. K. Samusev, C. Ruppert, N. Balakrishnan, V. E. Gusev, A. V. Stier, J. J. Finley, M. Bayer, A. V. Akimov, Coherent phonons in van der Waals MoSe<sub>2</sub>/WSe<sub>2</sub> heterobilayers. *Nano Lett.* **23**, 8186–8193 (2023).
- S. Kusaba, H.-W. Lin, R. Tamaki, I. Katayama, J. Takeda, G. A. Blake, Terahertz sum-frequency excitation of coherent optical phonons in the two-dimensional semiconductor WSe<sub>2</sub>. *Appl. Phys. Lett.* **124**, 122204 (2024).
- X. Jin, V. Aglieri, Y. Jeong, A. Pezeshki, L. Skokan, M. Shagar, Y. Jia, P. Bianucci, A. Ruediger, E. Orgiu, A. Toma, L. Razzari, Enhanced terahertz spectroscopy of a monolayer transition metal dichalcogenide. *Adv. Funct. Mater.* **35**, 2419841 (2025).
- J. Zhou, H. Xu, Y. Shi, J. Li, Terahertz driven reversible topological phase transition of monolayer transition metal dichalcogenides. *Adv. Sci.* **8**, 2003832 (2021).
- V. Jelic, S. Adams, D. Maldonado-Lopez, I. A. Buliyaminu, M. Hassan, J. L. Mendoza-Cortes, T. L. Cocker, Terahertz field control of surface topology probed with subatomic resolution. *Nat. Photonics* **19**, 1048–1055 (2025).
- J. Shi, Y.-Q. Bie, A. Zong, S. Fang, W. Chen, J. Han, Z. Cao, Y. Zhang, T. Taniguchi, K. Watanabe, X. Fu, V. Bulovič, E. Kaxiras, E. Baldini, P. Jarillo-Herrero, K. A. Nelson, Intrinsic 1T' phase induced in atomically thin 2H-MoTe<sub>2</sub> by a single terahertz pulse. *Nat. Commun.* **14**, 5905 (2023).
- C. Roelcke, L. Z. Kastner, M. Graml, A. Biereder, J. Wilhelm, J. Repp, R. Huber, Y. A. Gerasimenko, Ultrafast atomic-scale scanning tunnelling spectroscopy of a single vacancy in a monolayer crystal. *Nat. Photonics* **18**, 595–602 (2024).
- D. M. Juraschek, S. F. Maehrlin, Sum-frequency ionic Raman scattering. *Phys. Rev. B* **97**, 174302 (2018).
- F. Giorgianni, M. Udina, T. Cea, E. Paris, M. Caputo, M. Radovic, L. Boie, J. Sakai, C. W. Schneider, S. L. Johnson, Terahertz dispersive excitation of a coherent Raman-active phonon in V<sub>2</sub>O<sub>3</sub>. *Commun. Phys.* **5**, 103 (2022).
- H. Handa, Y. Okamura, R. Yoshimi, A. Tsukazaki, K. S. Takahashi, Y. Tokura, Y. Takahashi, Terahertz field driven giant nonlinear phonon response in ferroelectric semiconductor In-doped (Sn,Pb)Te. *Phys. Rev. B* **109**, I081102 (2024).
- S. Maehrlin, A. Paarmann, M. Wolf, T. Kampfrath, Terahertz sum-frequency excitation of a Raman-active phonon. *Phys. Rev. Lett.* **119**, 127402 (2017).
- M. Hase, M. Kitajima, Interaction of coherent phonons with defects and elementary excitations. *J. Condens. Matter Phys.* **22**, 073201 (2010).
- T. L. Cocker, V. Jelic, M. Gupta, S. J. Molesky, J. A. J. Burgess, G. D. L. Reyes, L. V. Titova, Y. Y. Tsui, M. R. Freeman, F. A. Hegmann, An ultrafast terahertz scanning tunnelling microscope. *Nat. Photonics* **7**, 620–625 (2013).
- T. L. Cocker, D. Peller, P. Yu, J. Repp, R. Huber, Tracking the ultrafast motion of a single molecule by femtosecond orbital imaging. *Nature* **539**, 263–267 (2016).
- H. Shigekawa, S. Yoshida, O. Takeuchi, Nanoscale terahertz spectroscopy. *Nat. Photonics* **8**, 815–817 (2014).
- V. Jelic, K. Iwaszczuk, P. H. Nguyen, C. Rathje, G. J. Hornig, H. M. Sharum, J. R. Hoffman, M. R. Freeman, F. A. Hegmann, Ultrafast terahertz control of extreme tunnel currents through single atoms on a silicon surface. *Nat. Phys.* **13**, 591–598 (2017).
- K. Yoshioka, I. Katayama, Y. Arashida, A. Ban, Y. Kawada, K. Konishi, H. Takahashi, J. Takeda, Tailoring single-cycle near field in a tunnel junction with carrier-envelope phase-controlled terahertz electric fields. *Nano Lett.* **18**, 5198–5204 (2018).
- S. Yoshida, H. Hirori, T. Tachizaki, K. Yoshioka, Y. Arashida, Z.-H. Wang, Y. Sanari, O. Takeuchi, Y. Kanemitsu, H. Shigekawa, Subcycle transient scanning tunneling spectroscopy with visualization of enhanced terahertz near field. *ACS Photonics* **6**, 1356–1364 (2019).
- T. L. Cocker, V. Jelic, R. Hillenbrand, F. A. Hegmann, Nanoscale terahertz scanning probe microscopy. *Nat. Photonics* **15**, 558–569 (2021).
- S. Yoshida, Y. Arashida, H. Hirori, T. Tachizaki, A. Taninaka, H. Ueno, O. Takeuchi, H. Shigekawa, Terahertz scanning tunneling microscopy for visualizing ultrafast electron motion in nanoscale potential variations. *ACS Photonics* **8**, 315–323 (2021).
- S. Sheng, M. Abdo, S. Rolf-Pissarczyk, K. Lichtenberg, S. Baumann, J. A. J. Burgess, L. Malavolti, S. Loth, Terahertz spectroscopy of collective charge density wave dynamics at the atomic scale. *Nat. Phys.* **20**, 1603–1608 (2024).
- K. Kimura, R. Tamaki, M. Lee, X. Ouyang, S. Kusaba, R. B. Jaculbia, Y. Kawada, J. Jung, A. Muranaka, H. Imada, I. Katayama, J. Takeda, Y. Kim, Ultrafast on-demand exciton formation in a single-molecule junction by tailored terahertz pulses. *Science* **387**, 1077–1082 (2025).
- J. Allerbeck, L. Bobzien, N. Krane, S. E. Ammerman, D. E. C. Figueroa, C. Dong, J. A. Robinson, B. Schuler, Ultrafast Coulomb blockade in an atomic-scale quantum dot. *arXiv:2412.13718 [cond-mat.mes-hall]* (2024).
- L. Wang, Y. Xia, W. Ho, Atomic-scale quantum sensing based on the ultrafast coherence of an H<sub>2</sub> molecule in an STM cavity. *Science* **376**, 401–405 (2022).
- V. Jelic, S. Adams, M. Hassan, K. Cleland-Host, S. E. Ammerman, T. L. Cocker, Atomic-scale terahertz time-domain spectroscopy. *Nat. Photonics* **18**, 898–904 (2024).
- S. Sheng, A.-C. Oeter, M. Abdo, K. Lichtenberg, M. Hentschel, S. Loth, Launching coherent acoustic phonon wave packets with local femtosecond coulomb forces. *Phys. Rev. Lett.* **129**, 043001 (2022).
- Z. Guguchia, A. Kerelsky, D. Edelberg, S. Banerjee, F. von Rohr, D. Scullion, M. Augustin, M. Scully, D. A. Rhodes, Z. Sheradini, H. Luetkens, A. Shengelaya, C. Baines, E. Morenzoni, A. Amato, J. C. Hone, R. Khasanov, S. J. L. Billinge, E. Santos, A. N. Pasupathy, Y. J. Uemura, Magnetism in semiconducting molybdenum dichalcogenides. *Sci. Adv.* **4**, eaat3672 (2018).
- I. G. Lezama, A. Ubaldini, M. Longobardi, E. Giannini, C. Renner, A. B. Kuzmenko, A. F. Morpurgo, Surface transport and band gap structure of exfoliated 2H-MoTe<sub>2</sub> crystals. *2D Mater.* **1**, 021002 (2014).
- H. C. Diaz, Y. Ma, R. Chaghi, M. Batzill, High density of (pseudo) periodic twin-grain boundaries in molecular beam epitaxy-grown van der Waals heterostructure: MoTe<sub>2</sub>/MoS<sub>2</sub>. *Appl. Phys. Lett.* **108**, 191606 (2016).
- H. Zhu, Q. Wang, L. Cheng, R. Addou, J. Kim, M. J. Kim, R. M. Wallace, Defects and surface structural stability of MoTe<sub>2</sub> under vacuum annealing. *ACS Nano* **11**, 11005–11014 (2017).
- K.-L. Yeh, M. C. Hoffmann, J. Hebling, K. A. Nelson, Generation of 10 μJ ultrashort terahertz pulses by optical rectification. *Appl. Phys. Lett.* **90**, 171121 (2007).
- M. C. Hoffmann, K.-L. Yeh, J. Hebling, K. A. Nelson, Efficient terahertz generation by optical rectification at 1035 nm. *Opt. Express* **15**, 11706–11713 (2007).
- J. Hebling, K.-L. Yeh, M. C. Hoffmann, B. Bartal, K. A. Nelson, Generation of high-power terahertz pulses by tilted-pulse-front excitation and their application possibilities. *J. Opt. Soc. Am. B* **25**, B6 (2008).
- M. Müller, N. Martín Sabanés, T. Kampfrath, M. Wolf, Phase-resolved detection of ultrabroadband THz pulses inside a scanning tunneling microscope junction. *ACS Photonics* **7**, 2046–2055 (2020).
- S. Sheng, L. Chen, J. Schust, K. Lichtenberg, M. Abdo, F. Huber, S. Baumann, S. Loth, Control of surface plasmon propagation and terahertz near-field waveforms in a scanning tunneling microscope. *Nano Lett.* **24**, 15291–15299 (2024).
- N. Martín Sabanés, F. Krecinic, T. Kumagai, F. Schulz, M. Wolf, M. Müller, Femtosecond thermal and nonthermal hot electron tunneling inside a photoexcited tunnel junction. *ACS Nano* **16**, 14479–14489 (2022).
- S. E. Ammerman, V. Jelic, Y. Wei, V. N. Breslin, M. Hassan, N. Everett, S. Lee, Q. Sun, C. A. Pignedoli, P. Ruffieux, R. Fasel, T. L. Cocker, Lightwave-driven scanning tunnelling spectroscopy of atomically precise graphene nanoribbons. *Nat. Commun.* **12**, 6794 (2021).
- L. Wimmer, G. Herink, D. R. Solli, S. V. Yalunin, K. E. Echterkamp, C. Ropers, Terahertz control of nanotip photoemission. *Nat. Phys.* **10**, 432–436 (2014).

45. R. Feenstra, A prospective: Quantitative scanning tunneling spectroscopy of semiconductor surfaces. *Surf. Sci.* **603**, 2841–2844 (2009).
46. A. P. Wijnheijmer, J. K. Garleff, K. Teichmann, M. Wenderoth, S. Loth, P. M. Koenraad, Single Si dopants in GaAs studied by scanning tunneling microscopy and spectroscopy. *Phys. Rev. B* **84**, 125310 (2011).
47. D. Peller, C. Roelcke, L. Z. Kastner, T. Buchner, A. Neef, J. Hayes, F. Bonafé, D. Sidler, M. Ruggenthaler, A. Rubio, R. Huber, J. Repp, Quantitative sampling of atomic-scale electromagnetic waveforms. *Nat. Photonics* **15**, 143–147 (2021).
48. H. Hirori, K. Shinokita, M. Shirai, S. Tani, Y. Kadoya, K. Tanaka, Extraordinary carrier multiplication gated by a picosecond electric field pulse. *Nat. Commun.* **2**, 594 (2011).
49. C. Lange, T. Maag, M. Hohenleutner, S. Baierl, O. Schubert, E. R. J. Edwards, D. Bougeard, G. Woltersdorf, R. Huber, Extremely nonperturbative nonlinearities in GaAs driven by atomically strong terahertz fields in gold metamaterials. *Phys. Rev. Lett.* **113**, 227401 (2014).
50. G. Froehlicher, E. Lorchat, F. Frenière, C. Joshi, A. Molina-Sánchez, L. Wirtz, S. Berceauid, Unified description of the optical phonon Modes in *N*-layer MoTe<sub>2</sub>. *Nano Lett.* **15**, 6481–6489 (2015).
51. M. Grzeszczyk, K. Gołasa, M. Zinkiewicz, K. Nogajewski, M. R. Molas, M. Potemski, A. Wyszomolek, A. Babiński, Raman scattering of few-layers MoTe<sub>2</sub>. *2D Mater.* **3**, 025010 (2016).
52. Q. J. Song, Q. H. Tan, X. Zhang, J. B. Wu, B. W. Sheng, Y. Wan, X. Q. Wang, L. Dai, P. H. Tan, Physical origin of Davydov splitting and resonant Raman spectroscopy of Davydov components in multilayer MoTe<sub>2</sub>. *Phys. Rev. B* **93**, 115409 (2016).
53. M. Yamamoto, S. T. Wang, M. Ni, Y.-F. Lin, S.-L. Li, S. Aikawa, W.-B. Jian, K. Ueno, K. Wakabayashi, K. Tsukagoshi, Strong enhancement of Raman scattering from a bulk-inactive vibrational mode in few-layer MoTe<sub>2</sub>. *ACS Nano* **8**, 3895–3903 (2014).
54. T. Wieting, A. Grisel, F. Lévy, Interlayer bonding and localized charge in MoSe<sub>2</sub> and  $\alpha$ -MoTe<sub>2</sub>. *Phys. B+C* **99**, 337–342 (1980).
55. Y.-X. Yan, E. B. Gamble, K. A. Nelson, Impulsive stimulated scattering: General importance in femtosecond laser pulse interactions with matter, and spectroscopic applications. *J. Chem. Phys.* **83**, 5391–5399 (1985).
56. L. Dhar, J. A. Rogers, K. A. Nelson, Time-resolved vibrational spectroscopy in the impulsive limit. *Chem. Rev.* **94**, 157–193 (1994).
57. H. J. Zeiger, J. Vidal, T. K. Cheng, E. P. Ippen, G. Dresselhaus, M. S. Dresselhaus, Theory for dispersive excitation of coherent phonons. *Phys. Rev. B* **45**, 768–778 (1992).
58. T. Huber, M. Ranke, A. Ferrer, L. Huber, S. L. Johnson, Coherent phonon spectroscopy of non-fully symmetric modes using resonant terahertz excitation. *Appl. Phys. Lett.* **107**, 091107 (2015).
59. Z. Fu, M. Yamaguchi, Coherent excitation of optical phonons in GaAs by broadband terahertz pulses. *Sci. Rep.* **6**, 091107 (2016).
60. T. Shimada, F. S. Ohuchi, B. A. Parkinson, Work function and photothreshold of layered metal dichalcogenides. *Jpn. J. Appl. Phys.* **33**, 2696 (1994).
61. L. A. H. Jones, Z. Xing, J. E. N. Swallow, H. Shiel, T. J. Featherstone, M. J. Smiles, N. Fleck, P. K. Thakur, T.-L. Lee, L. J. Hardwick, D. O. Scanlon, A. Regoutz, T. D. Veal, V. R. Dhanak, Band alignments, electronic structure, and core-level spectra of bulk molybdenum dichalcogenides (MoS<sub>2</sub>, MoSe<sub>2</sub>, and MoTe<sub>2</sub>). *J. Phys. Chem. C* **126**, 21022–21033 (2022).
62. N. Krane, C. Lotze, N. Bogdanoff, G. Reecht, L. Zhang, A. L. Briseno, K. J. Franke, Mapping the perturbation potential of metallic and dipolar tips in tunneling spectroscopy on MoS<sub>2</sub>. *Phys. Rev. B* **100**, 035410 (2019).

**Acknowledgments:** We thank S. Loth and T. Cocker for valuable discussions. **Funding:** K.J.F. and T.K. acknowledge financial support by the Deutsche Forschungsgemeinschaft (DFG, German Research Foundation) through project no. 328545488 (CRC 227, project no. B05).

**Author contributions:** V.N.R., C.L., and K.J.F. conceived the idea. V.N.R., J.S., and P.W. carried out the measurements. N.B., C.L., V.N.R., and S.T. with the advice of T.S.S. and T.K. set up the THz-STM. V.N.R., F.F., and J.S. performed the data analysis. V.N.R., J.S., F.F., N.B., S.T., P.W., T.S.S., T.K., C.L., and K.J.F. discussed the results. V.N.R., F.F., and K.J.F. wrote the manuscript with input from J.S. and C.L. **Competing interests:** The authors declare that they have no competing interests. **Data and materials availability:** All data needed to evaluate the conclusions in the paper are present in the paper and/or the Supplementary Materials. The raw data is available at <https://doi.org/10.5281/zenodo.17649845>.

Submitted 10 June 2025

Accepted 12 November 2025

Published 12 December 2025

10.1126/sciadv.adz6549